The Contact Mechanics of a UK Railway Ballast

Cacin P.Y. Wong* & Matthew R. Coop[+]

* Anglia Ruskin University, formerly University College London

+ University College London

Abstract

A newly developed apparatus was used to investigate the contact mechanics between particles of a common UK railway ballast. The data were then compared with the models currently and commonly used in geotechnical DEM analyses but the discrepancy between the predictions and measurements is large even at small loads. The first contact behaviour was much softer than the Hertz-Mindlin model for smooth spheres, both in normal and shear. Even if the normal loading could be fitted better with a model that accounted for roughness, the elastic nature of these models could not capture the plasticity that is evident on unloading. Large displacement shear cycles caused not only an increase of inter-particle friction as discussed previously, but also a significant degree of particle interlock arising from the wear of the contacts. While there were no rate effects for sliding shearing, contact ageing displacements could be observed at pre-failure loads, although these stabilised after a few days. Pre-failure cyclic loading resulted in stiffnesses that increased in lateral loading but decreased in normal loading, but in both cases stabilised after a few tens of cycles, while the stiffnesses at the reversals of the large displacement cycles did not evolve with continued cycling. The presence of water did not affect the lateral stiffness and the influence of the normal load was consistent with Hertz-Mindlin, even if the absolute values were much softer. It can be concluded that the current commonly used models for DEM analyses are not applicable for ballast/crushed rock and alternate models should also focus on plasticity at the asperity scale.

Keywords: Laboratory Tests, Granular Materials, Particle-Scale Behaviour, Rocks/Rock Mechanics, Stiffness

Introduction

Continuum models of soil behaviour have become ever more complex, but still struggle to cope with the multiple factors that influence soil behaviour; plasticity, the influence of stress history, anisotropy, effects of stress rotation, the influence of the intermediate principal stress, particle breakage, rate effects and creep, the influence of natural structure, etc. The alternative is to use discrete models, such as Discrete Element Modelling (DEM). Often this is however, based simply on the use of unrealistic spherical elements in which case there is little need to know the contact mechanics of the particles involved. The "correct" input parameters are in that case simply those that give the best curve fitting to some test data at the continuum scale, for example a triaxial test. Contact parameters derived like this are likely to bear little resemblance to reality.

As computing power increases it may soon become feasible to make a one-to-one or Avatar model at least for coarse-grained soils. Such a model will require the correct particle shapes, the correct micromechanics of the particles, notably the correct contact behaviour, and the correct fabric i.e. an arrangement of the particles and their contacts that is the same as that in the engineering design. Modelled particle shapes are now becoming ever more realistic (e.g. Fellerec & McDowell, 2010) and the measurement of the fabrics of coarse-grained soils from sands to ballasts is now routine (e.g. Le Pen et al., 2014). But if we want to move to a real Avatar DEM model with the correct fabric, particle sizes and shapes then it becomes imperative also to have a model of the contact mechanics within the DEM that allows us to capture the key aspects of the contact behaviour that we anticipate will affect the macro (or more correctly meso) -scale soil behaviour.

Railway ballast offers perhaps an easier first step in the creation of realistic DEM models. This is because the number of particles is relatively small and at the typical stress levels imposed there would be expected to be limited particle crushing, which would add the complication of redefining the particles and their contacts as the breakage occurs. As an engineered material the ballast will have also a simple structure defined only by the fabric created at placement. The work presented in this paper therefore examines in detail the contact behaviour of a typical ballast.

Apparatus have been built to investigate particle contact mechanics since the 1960s, initially focusing only on the measurement of the coefficient of inter-particle friction (e.g. Skinner, 1969, Proctor & Barton, 1974), but more recently moving on to examining the contact

stiffnesses, at first with simple tests (e.g. Cavarretta et al., 2011) but now with more sophisticated apparatus and techniques, with greatly improved accuracy. Typically, the apparatus used have been developed to investigate particular types of loading and do not have the freedom to control all the possible forces and/or displacements at particle contacts (e.g. Michalowski et al., 2018; Cole & Peters, 2007) but Nardelli & Coop (2019) built a three-axis inter-particle loading apparatus that gives complete control in three dimensions. This apparatus design was adapted by Wong et al. (2018) for the larger forces applied to large-sized grains, developing an apparatus that is suitable for particles from gravel size to smaller rock fill.

There are still a limited number of investigations of contact mechanics, more on sands (e.g. Cavarretta et al., 2011; Nardelli et al., 2017; Nardelli & Coop, 2019: Cole, 2015) but fewer for larger grains and many more for normal loading than for combined normal and tangential loading. Tapias et al. (2015) carried out simple contact tests on a limestone rock fill, while Cole & Peters (2007) and Cole et al. (2010) investigated aspects of the contact behaviour of a gneiss, some for its "natural" shape as a crushed rock and others for simpler shapes such as spheres and flat surfaces. Their work in shearing was limited to low load levels.

While there are a reasonable number of investigations of individual aspects of behaviour on various grain types there are few comprehensive studies of multiple aspects of behaviour on one material. Typical conclusions for various grain types have been that in normal loading, the response at higher loads often tends to be similar to a Hertzian (1882) response but softer at small load levels (Cole, 2015; Nardelli et al, 2019), while Nardelli & Coop found that an existing variant of the Hertz model that is modified to account for the surface roughness (Greenwood et al., 1984) fitted the data well, at least for more spherical particles of a quartz sand. For a quartz sand, Michalowski et al. (2018) highlighted that creep, or more correctly contact ageing effects were significant in normal loading.

Rather less work has been done on tangential loading stiffness, and that has mostly been on regular shapes. The behaviour is highly non-linear with stiffnesses that increase with the applied normal load (Cole et al., 2010; Senetakis et al., 2013), but Nardelli & Coop (2019) found that the Mindlin & Deresiewicz (1953) model, which like Hertz (1882) is based on the deformation at the contact of elastic spheres, overestimated the tangential stiffnesses by a factor of around two. Coefficients of friction, μ measured during sliding failure are highly variable, even for one material, but Nardelli & Coop showed that for sands of various mineralogies it was the particle roughness that was important, not larger-scale aspects of morphology such as

roundness or sphericity. Values of μ for various materials were found by Cole (2015) to vary with load level, some increasing and some decreasing, but testing over a wider range of loads and a greater variety of sand mineralogies Nardelli & Coop (2019) only found small effects.

Much existing work tends to have been fragmented in nature and there are few comprehensive investigations on grains of natural shapes, fewer on larger grains such as ballast or rock fill, of which even fewer are at the higher contact loads that those materials might encounter. This paper describes an investigation of the contact mechanics of one of the most commonly used UK railway ballasts, the future aim of the work being to create an accurate DEM model in collaboration with partners at the universities of Nottingham and Southampton that will include both accurate particle shapes and fabric of the ballast assembly. In this paper, normal and tangential load-deflection behaviour are compared to some models available in the literature. The choice of contact models is potentially very wide, but only those already used in applications within Geotechnical modelling have been considered, although almost entirely without measured contact mechanics. The intention here is not to call into question the models, which have been applied with success to other materials, but merely to highlight the practical difficulties we will face in applying them to the discrete analysis of soil behaviour, in this case, a railway ballast.

Apparatus and Ballast Tested

A general view of the apparatus is given in Fig.1. The apparatus has been described elsewhere (Wong et al., 2018) and so only brief details are given here. The two particles whose contact is to be tested are glued to platens, with the contact location concentric with the axes of the three loading systems. The loads and/or displacements are applied by linear actuators and measured with load cells and proximity transducers aimed at targets on the sled that carries the bottom platen. Apart from the large capacity of 1kN in normal load, the other key innovation in this apparatus is the use of a new capacitive form of proximity transducer to measure the displacements, which was found to perform slightly better than the more traditional eddy current types. For small load or displacement changes, for example, when measuring the contact stiffnesses, the displacements and loads have precisions of about 0.01μm and 0.01N. The sled is free moving, being supported on a three-point bearing system, the friction of which was negligible for the load levels used here.

The material tested is a common UK granite (or more accurately granodiorite) ballast from the Mountsorrel quarry in Leicestershire, supplied by the University of Nottingham who use it extensively in model testing of rail tracks. The ballast was tested in its "as supplied" state as it would be used in UK rail track, and being simply a crushed and graded rock it has angular particles. Two particles are shown mounted on the platens in Fig.1b. The lower particle was typically a nominal flat, although the surface was the natural, as supplied broken rock surface, while the top particle was a nominal point. Since the contact behaviour should not be significantly influenced by deformations in the bulk of the particles, it is not necessary to have the entire particles in the apparatus and sections have been cut from the full-sized particles. Both are glued to the platens with epoxy resin, but the glued surfaces were machined flat and the glue thickness was also kept small (about 0.15mm) to minimise compliance. The flexibility of the apparatus, including the glued contact, was measured and deducted from all displacements, but it was small relative to the measurements made.

The use of a point-to-flat contact contrasts with the more spherical particle-to-particle sand contacts used by Nardelli & Coop (2019). However, any attempt to compare the data from the tests with theoretical models, requires a nominal single contact, which means testing either point-to-point, point-to-edge or point-to-flat contacts. Any other configuration, for example, nominal flat-to-flat or edge-to-flat, would necessarily have multiple contact locations even at the macro scale making any comparison with models impossible. It would also invalidate the design of the apparatus since the direction of the applied forces might not be coincident with its axes. Within an assembly of angular particles of this type, point-to-flat contacts would also be more common than other contact types. Technically these tests were very much more difficult to carry out than those on rounded and spherical particles and using point-to-flat minimised those difficulties. While at the macro scale we might refer to a particle "point" it is clear from Fig.1 that the particles supplied from the quarry actually do not have sharp points and it would be inappropriate to use, for example, a contact model for a true point-to-flat contact. Instead, the contact has been considered as a rough sphere-to-flat.

Details of the tests are given in Table 1. The normal load levels chosen of 20-200N were based on typical ranges of contact forces in Nottingham University DEM analyses of full-scale model tests of rail track and of triaxial tests. Higher loads would also have led to major particle damage, and it was intended that this investigation should be restricted only to forms of particle damage that do not significantly affect the overall particle shape.

Detailed results from cyclic sliding tests carried out on this ballast to measure the coefficient of friction μ were reported by Wong & Coop (2020) and any repetition here will be minimised. The key conclusions of that work were that for large displacement cycles the μ values increase as the cycling continued, but while μ increased the abrasion reduced the RMS roughness of the surfaces. The μ values were not affected by the normal load level or the presence of the ground powder created at the contact, but were significantly reduced in the presence of water, in contrast to the observations of Nardelli & Coop (2019) for sands.

Monotonic Normal Loading

The first stage of the tests was normal loading and a summary of the data from 11 tests is given in Fig.2. Even if the data for a few tests have been truncated when any major particle damage event occurred, there is still considerable scatter. Comparisons are made with a few published data. The Leighton Buzzard quartz sand particles (LBS) from Nardelli & Coop (2019) were all approximately spherical and had diameters in the range of 1.2-5mm. It is interesting that the ballast particles that have much larger nominal sizes (D_{50} =39mm) have a softer normal loading response, even if the mineralogy is still dominated by quartz. Also shown are data for a completely decomposed granite (Nardelli & Coop, 2019). These 2.4-5mm particles had been washed to remove their weathered coating (denoted WCDG) and the remaining grains would have broadly similar mineralogy to the fresh granite used here. Again, given the much smaller size, the similar contact stiffnesses for the WCDG may seem surprising. Lastly, the maximum and minimum responses for a number of tests on machined 14.7mm spheres of another igneous rock, gneiss, are shown from Cole et al. (2010) and these are very much stiffer.

The contact radii of the upper particle were measured using the two orthogonal microscope cameras shown in Fig.1a, one in the direction of the applied shear displacements and one perpendicular. Circles were manually fitted within the two images to estimate the contact radii, an example of which is shown in Fig.1b, and a mean taken, the two values typically being similar, as can be seen in Table 1. In a few cases, the images that could be obtained from the cameras did not allow the contact radius to be established in one or another direction. The lower particle was taken as flat, i.e. infinite radius.

The measured contact radii of the upper particle are indicated in Fig.2. It might have been expected that the large scatter in the data could have resulted from different radii, but there is no clear correlation with the force-displacement relationship. The upper particles were

randomly selected within what might be described as a particle point or apex, and it is interesting how the upper particle contact radii are quite similar. The contact radius that can be measured in the example in Fig.1b seems fairly clear, so this must be an indication that the behaviour is influenced by features of the contact at a smaller scale than can be seen by the microscope camera. Ideally, this should be investigated with X-Ray CT, which would reveal the morphology within the contact area and with greater resolution than from an external view like the microscope cameras. However, carrying out contact loading tests of this nature and accuracy within a CT scanner is, as yet, unfeasible.

The large scatter of the data would also raise an obvious question about how many tests would be needed to be representative, an issue that would need DEM analyses to investigate how these discrepancies at the micro-scale would influence behaviour at the macro. Carrying out a much greater number of tests than were done here would start to become prohibitively time-consuming.

Normal stiffnesses have been calculated by linear regression over short intervals of the force; displacement curves (Fig.3). The relationship on the log stiffness: log displacement graph is quite consistent with the increase of stiffness expected from the enlarging contact area of smooth spheres of Hertz (1882) having a gradient of around 0.5, although it will be shown below that the absolute values of predicted displacement are in poor agreement.

Comparisons with existing contact theories require the Young's modulus, E, and a value of about 70GPa may be estimated for various granites (Vasconcelos et al., 2008; Domede et al.; 2019), which broadly agrees with the constituent mineral Young's moduli of quartz, orthoclase feldspar and plagioclase feldspar, which range between 40-100 GPa (Brace, 1965; Mavko et al., 2009; Jaeger et al., 2009). A uniaxial loading test on a small cylindrical sample cut from a ballast particle confirmed the value of 70 GPa but was not sufficiently repeatable to be able to refine the value further. The Poisson's ratio (v) of granite has been measured as 0.20-0.28 (Domede et al., 2019; Chen et al., 2014; Jaeger et al., 2009) and a value of 0.25 has been assumed here.

Hertzian theory was developed for the contact of two smooth spheres, not necessarily of the same radius, between two materials that also are not necessarily the same. It assumes that all the displacement is in the contact region and that there is none in the bulk of the sample. The mutual approach of the centres of the two spheres, δ, is then given by:

$$\delta = \frac{a_H^2}{R} = \left(\frac{9N^2}{16RE^{*2}}\right)^{1/3} \qquad (1)$$

where a_H is the radius of the contact area and N is the normal contact force. As the force increases the area of contact increases, and so the contact stiffness increases, giving an exponential curve in which the force is proportional to the displacement to the power of 2/3, the relationship also depending on the Young's modulus and the two contact radii. The equivalent radius R is given by $1/R = 1/R_1 + 1/R_2$ where R_1 and R_2 are the radii of the two spheres and the equivalent elastic modulus E^* is taken as $1/E^* = (1-v_1^2)/E_1 + (1-v_2^2)/E_2$ in which v_1, E_1, v_2 and E_2 are the Poisson's ratios and Young's moduli of the two materials.

The apparent contact area between two rough spheres will be larger than that for smooth ones, although the true contact will only be over a smaller area at the asperities. Greenwood et al. (1984) introduced a normalised asperity size, α, the normalisation being with respect to the mutual displacement and hence to the sizes of the spheres and the materials from which they are made:

$$\alpha = \frac{\sigma R}{a_H^2} \qquad (2)$$

where σ is the combined roughness of the two materials, $\sigma = (S_{q1}^2 + S_{q2}^2)^{1/2}$ in which S_{q1} and S_{q2} are the root mean square roughnesses once the shape of the spheres has been removed from the profile. In this model, the asperities are assumed to be spherical in shape behaving in a Hertzian manner. Based on experimental data for the contact areas between metal surfaces of Johnson (1985), Yimsiri and Soga (2000) proposed an empirical equation to relate the radius of the contact area in Hertz, a_H to that of the new apparent contact area a^*, which could then replace a_H in the Hertzian Equation 1:

$$\frac{a^*}{a_H} = \frac{-2.8}{\alpha+2} + 2.4 \qquad (3)$$

Hertz predictions are shown in Fig.4a. Even if the upper particle contact radii are generally quite similar in the two orthogonal directions in Table 1, there are larger differences between different particles, and so on Fig.4a predictions are shown for the maximum upper particle contact radius, 4.4mm, the minimum, 1mm, and the mean, 2mm. None come remotely close to the real data, and a best-fit curve could only be obtained either by adopting a tiny upper particle contact radius of 50μm or an improbably low E of 11GPa. The very small radius that would be

required to fit the data is again an indication that features much smaller than are visible with the microscope cameras control the contact behaviour and that will include the particle roughness.

For predictions using the Greenwood et al. (1984) model, the RMS roughnesses, S_q, were measured with a Zeiss Stereo-Discovery V8 optical microscope. In previous work for smaller, smoother particles (e.g. Nardelli & Coop, 2019), white light interferometry was used to measure the particle roughness, but this technique cannot cope with the very much larger roughnesses of the ballast. A Z-stack reconstruction was made from multiple images taken at different heights and then the three-dimensional surface was reconstructed with ConfoMap7 adapted for Zeiss from the Mountains range of software. To measure the roughness a polynomial function was fitted to the surface within the software so that the form could be removed and the surface flattened. Waviness and noise were reduced with Gaussian filters. Roughness values will vary slightly with the field of view so for consistency a field of view of 0.2 mm x 0.2 mm was chosen based on the order of magnitude of the Hertz prediction of the contact area. This resulted in an image resolution of 0·65 μm in the vertical direction. Four images of upper particles and four of lower ones gave values of S_q between 5.2-25.3μm with a mean of 18.2μm. The predictions from the Greenwood et al. method are referred to as Hertz* in Fig.4b and as Nardelli & Coop (2019) found for a quartz sand, they are much better than Hertz.

There are several problems in applying the Greenwood et al. / Yimsiri & Soga model. The first is that it is intended for spherical particles. While the lower particle can be assumed to be flat, and so a sphere with infinite radius, the upper particle is very clearly not a sphere. As discussed above, the contact displacements should not have any component from the bulk of the particle and, as a first approximation, the shape at the contact that is visible in Fig.1b does fit a circle well, but it is possible that the assumption of a sphere for the top particle could be contributing towards discrepancies between experimental data and theoretical predictions. Secondly, the values of α are large, reducing from around 15 at 10μm displacement to around 3.7 at 40μm. While Yimsiri and Soga plotted their hyperbolic relationship between α and a^*/a_H up to an α of 10, the data from Johnson (1985) used to validate it stop at α values of around 1, so the use of their relationship for larger values is uncertain. More experimental data for higher α values and for geological materials rather than hardened steel are badly needed.

Using the Yimsiri & Soga definition of α (Eqn 3), at large displacements, the tangent normal stiffness should tend towards that of Hertz as a^*/a_H tends to 1. This was seen by Nardelli & Coop for a quartz sand. However, at larger loads the Greenwood et al. predictions for the more angular ballast tend to be too stiff, which is probably the result of plasticity at the contact, as can be seen from the unload-reload cycles for Test SC15 in Fig.4c. This plasticity was much greater than was seen for the sand and so the elastic formulation of Greenwood et al. and Hertz is therefore a severe limitation for such a material.

For a smooth sphere-to-sphere contact, Hertz gives the maximum stress at the contact as:

$$\sigma_{max} = \left(\frac{6NE^{*2}}{\pi^3 R^2}\right)^{1/3} \qquad (4)$$

For sphere-to-flat contact Tabor (1951) suggests that the yield stress will be about 60% of the hardness, and for Mountsorrel granite Afrouz (1992) measured a hardness of 6.3GPa, giving a yield stress of about 3.8GPa. This would lead to an estimate of the load at the onset of yield for a 2mm radius upper particle of 815N. This is well beyond the loads actually applied in these tests and far above the loads of around 20-30N when the data start to become significantly softer than the Greenwood et al. predictions. This is another indication that it is behaviour at the micro-scale and probably plasticity in the asperities that is dominating the behaviour. The onset of that plasticity seems to be gradual as the data show no clear yield or inflection in the data just a gradual divergence from the predictions. It also emphasises that elastic contact models, even accounting for roughness, may not be appropriate for these very rough geomaterials and future research should examine the use of models accounting for plasticity at the contact.

At smaller loads, when the mean upper particle contact radius (2mm) is used the Greenwood et al. predictions are at the lower bound of the data and only the largest measured value (4.4mm) gives a more reasonable fit (Fig.4b). If the actual size of the upper particle is input, rather than the contact radius, using a mean of 7.1mm, then the predictions plot at the upper end of the data. However, particle size should be irrelevant, and it is only the contact radius that should govern the stiffness. Although plasticity at the contact is confirmed by the test data, there was never any very clearly visible damage or plasticity in the loading area of either particle in normal loading for the load levels in Fig.4, the data being discontinued if any more major damage was suspected. There was also no clear damage in shear except when large numbers of large shear displacement cycles were applied (see Wong & Coop, 2020) and so it can be

inferred that the plasticity and/or other damage such as fracturing was at too small a scale to be visible. Ideally, the contact morphology and any changes to it during loading that could explain the observed plasticity should be measured at the precise location of the contact between the two particles, but this would again require X-Ray CT.

Contact Ageing

The continued positive displacements at the top of the unload-reload loops in Fig.4c indicate some effects of creep, or contact ageing, as the loading was stopped, and the unloading started. It is not present at the bottom of the loops where the load is close to zero. These effects were investigated more systematically in two tests that were carried out on the same contact firstly under normal loads only and then with a combined normal and shear load. In each case, the loads were applied as rapidly as possible, in a few seconds, and the zero time of the graphs corresponds to the time when the new force was reached. The data in Fig.5a indicate that at 55N normal load there is very little creep, about 1μm, which is less than was evident for Test SC15 in Fig.4c, but the amount is likely to depend on the contact morphology at the micro-scale (i.e. the asperities). At 200N it is much more significant at about 8μm, but in both cases, it stabilises after a few days. Michalowski et al. (2018) observed displacements an order of magnitude smaller for single quartz sand grains normally loaded between platens under correspondingly smaller forces, but these also stabilised in a few days. They noted that the contact ageing displacements depended on the roughness, and this is likely to be the cause of the larger displacements seen for the ballast. A shear force of 100N was then applied, designed to be a large shear to normal force T/N ratio but without risking sliding failure (Fig.5b). The additional vertical contact displacement under the combined load was then only about 3μm while the much larger horizontal displacement of 10-11μm stabilised relatively quickly, in a few hours. Michalowski et al. speculated that the contact maturing effects they observed were the result of time-dependent fracturing at the micro-scale but it could equally well be attributed to time dependency of the plastic flow at the asperities.

Monotonic and Cyclic Sliding Failure

The final stage of most tests was a large displacement, ±1mm, cyclic shear loading and selected cycles from a typical test are shown in Fig.6; some stick-slip events where the contact was not

at sliding failure have been removed for clarity. The data have been corrected for any slight gradient of the interface, by plotting shear force T and normal force N which are derived by resolving the measurements made of the horizontal and vertical forces, using the gradient taken from a plot of the vertical displacements against the horizontal displacements. However, the correction is small. The cycling started at +1mm and was generally at 30 mins per cycle. Prior to the cycling, a linear shear stage was carried out from 0mm, the point of initial contact, to +1mm. This was done slightly more slowly and more carefully, at a shearing rate of 1-2mm/hour, so that sufficient data could be retrieved to define the stiffness accurately. The large cycle sizes were applied to ensure that on each cycle gross sliding was achieved and it can be seen that on each reversal of direction the T/N values stabilise after about 200μm. The cycles were applied by using a displacement control in the horizontal loading system so they are unaffected by whatever the resulting forces are.

As Wong & Coop (2020) highlighted, the values of T/N at sliding failure (μ) tend to increase during cycling and this is clearer in Fig.7a which shows average μ values. All the data from 15 tests on dry contacts are shown, and the figure presented by Wong & Coop (2020) has been modified by adding the μ for the initial linear shear, taken as an average value between when T/N stabilises at around 200μm horizontal displacement and 1mm. Because of the log scale, this is shown as Cycle 1, while the start of the true cycling is from Cycle 2 onwards. It is clear from Figs.6a and 7a that for Test SC13_b the μ value mobilised during the initial linear shear is lower than during subsequent cycles, but this does not result from the rate of shearing, as will be discussed below. The values of μ then increase more slowly from Cycle 2, mostly stabilising after around 100 cycles. Many of the tests in Fig.7a show similar trends, while some show little change in μ between the linear shear and the first cycles and some a small decrease. The μ values therefore are far more scattered for the first shearing and converge as cycling commences. This must be associated with the initial morphology of the contact surfaces and changes during the initial shearing, but as yet it is not possible to resolve the small changes in morphology that might be the cause. During the large displacement shear cycles, there was significant grinding at the particle contact and this has been discussed in detail by Wong & Coop (2020) and will not be repeated here. However, there was no clear visible damage for small displacements in shear or the pre-sliding cycles that are discussed below.

The linear shear μ values for the ballast are added in Fig.8 to the data presented by Nardelli & Coop (2019) for the effects of surface roughness of various sands they tested along with data for ceramic and steel balls from Cavarretta et al. (2010). The different colours of the Eglin sand

(Nardelli et al., 2017) indicate different minerals. Also added are data from glass ballotini from Cavarretta et al. (2010). While for the other materials only mean values are shown, because of the large variability for the ballast the range and mean of the µ values is shown plotted against the range and mean roughness of the ballast. The ballast fits within a trend of increasing µ with roughness, although this is not necessarily a linear trend even on the log roughness scale.

Development of Mechanical Interlock

It is clear from Fig.6b the vertical displacements do not cease as the top particle flattens and a slot is ground in the lower one. In Fig.6a it is evident that this wear gives rise to evolving peaks at the corners of the displacement cycles and for this reason, the µ values in Fig.7a are calculated only for the central 1mm portion of the shearing path. In Fig.7b these peaks are shown for selected cycles. The shear forces T are normalised with respect to the normal force N, but only for a comparison of data for different load levels; T/N at these peaks simply represents a developing interlock, not a value of µ. As the tests proceed, the values of T/N at the corners increase from being equal to µ at low numbers of cycles to much larger values, and within the data scatter it seems that this interlock is proportional to the normal load and seems also to stabilise at over 100 cycles. It should however be emphasised that this is only the interlock measured for a constant displacement cycle and the shear force that would be required to continue to larger displacements is likely to be larger.

Influence of Rate of Sliding

The influence of the rate of shearing on the mobilised coefficient of friction was investigated in Test SC14_b where the rate of displacement was varied during the cyclic shearing (Fig.9). Because of difficulties with control of the test as the particles dug into each other, the shearing path was shortened to ±0.6mm, but this does not affect the µ value that is calculated over the central 1mm. For Cycles 40 and 41, the rate of shearing was slowed from 0.5 to 50 hours/cycle; it was then increased back to the faster rate for Cycle 42 onwards. Neither step change of shearing rate has any effect on µ which agrees with what Nardelli & Coop found for a quartz sand. Others have found significant rate effects on µ for sands, although using other techniques (Kasyap & Senetakis, 2019).

Lateral Stiffness

The lateral load: displacement data for all tests for which good quality data were obtained are shown in Fig.10. A logarithmic horizontal displacement scale is used so that the data may be plotted from the smallest displacements up to sliding failure. The data have been normalised by dividing the T/N ratio by μ to account for differences in values at sliding failure that were evident in Fig.7a. Some of the tests do not start at zero shear load, T, because in applying the normal load, N, the contact geometry, even if nominally flat, had a local irregularity. The predictions from Mindlin and Deresiewicz (1953) are also shown in the figure. In this model an initial elastic lateral stiffness, K_{T0}, is calculated as an extension of Hertz, using the Hertzian contact area and imposing a lateral load:

$$K_{T0} = 8a_H (\frac{2-\nu_1}{G_1} + \frac{2-\nu_2}{G_2})^{-1} \qquad (4)$$

where G_1 and G_2 are the shear moduli of the two materials. The decay in stiffness from T/N=0 to T/N=μ is then non-linear and hysteretic but empirically based. It is hypothesised to result from micro-slip within the contacting area between the particles. The hysteresis is created by making the current stiffness K_T depend not only on the loading direction, but also on the magnitude of the shear force, T, relative to its value the last time there was a change from loading to unloading (or vice versa), T^*:

for increasing T and |T|≤|T*| $K_T = K_{T0}(1 - \frac{T-T^*}{2\mu N})^{1/3}$ $\qquad (5)$

for increasing T and |T|>|T*| $K_T = K_{T0}(1 - \frac{T}{\mu N})^{1/3}$ $\qquad (6)$

for decreasing T and |T|≤|T*| $K_T = K_{T0}(1 - \frac{T^*-T}{2\mu N})^{1/3}$ $\qquad (7)$

for decreasing T and |T|>|T*| $K_T = K_{T0}(1 + \frac{T}{\mu N})^{1/3}$ $\qquad (8)$

Mindlin and Deresiewicz predictions are shown for each load level, but even if the general shape of the curves is similar to the data, they are all one or two orders of magnitude too stiff, which is much worse than the factor of about two difference seen by Nardelli & Coop (2019) for much smoother and smaller quartz sand grains. Most of the predictions are shown for the mean measured contact radius of 2mm for the upper particle, but for 100N the effect of this radius is shown for the minimum measured value of 1mm but it has little effect compared to

the large differences with the data. Considering that Mindlin and Deresiewicz uses the Hertz contact area as its starting point, it is not perhaps surprising that the Mindlin and Deresiewicz predictions are incorrect, but what is perhaps worth remarking on is that the errors are very much larger than the factor of around four that was seen in Fig.4a between the normal loading measurements and Hertz predictions. One possible reason for this much larger discrepancy could be that for Hertz's theory in normal loading the equivalent radius means that two spheres do not need to be of equal size and one can even be flat. In contrast, Mindlin and Deresiewicz specifically defined their theory for two equal spheres. However, there is nothing in their assumptions that seems to preclude unequal spheres so that others (e.g. Vu-Quoc & Zhang, 1999) have since introduced the equivalent radius.

This large difference between the predictions and the data could again be the result of the effect of the roughness, which is not included in Mindlin and Deresiewicz. The greater effect of the roughness on the ballast compared to sands was also evident with the much poorer agreement in Fig.4a between the data and the Hertz predictions than was found for the quartz sand by Nardelli & Coop, and in the large effect that the roughness has in Greenwood et al. (1984) predictions in Fig.4b by comparison with Hertz in Fig.4a.

An assumption made by Otsubo et al. (2015) was that the ratio of the initial shear stiffness to the current normal stiffness at the applied normal load (K_T/K_N) would be the same for a rough surface as for the smooth surfaces assumed by Hertz-Mindlin. For a normal load of 100N and using the mean upper particle contact radius of 2mm, this would give the ratio of K_{T0}/K_{T0}^{*} of only 1.85 where K_{T0}^{*} is the initial shear stiffness for the rough surface. The ratio would remain constant during the stiffness degradation since the stiffness at any displacement is simply determined from the initial stiffness and the empirical decay. This estimate is also plotted in Fig.10 but it remains very far from the measurements. It is perhaps surprising that the attempt to include the effect of roughness makes so little impact on the discrepancy between the predictions and measurements, given that in normal loading the agreement with Greenwood et al. (1984) was so very much better than with Hertz, especially at lower loads. Even at 20N normal load which did not seem to be affected by plasticity in normal loading (Fig.4b), the discrepancy in tangential loading remains very high.

Tangent stiffnesses were calculated from these monotonic lateral loading tests by taking linear regressions through short intervals of the data, typically between 5 and 51 data points, out of a total of about 600 data points during the linear shear. The resulting stiffnesses (Fig.11) are

highly non-linear but clearly depend on the load level. The fluctuations of the stiffnesses in some tests result from some stick-slip due to local asperities.

Lateral stiffnesses could also be calculated from the reversals of the cyclic tests, but because the cyclic tests generated a very large amount of data (typically about 100000 lines) the number of data points at each reversal between the change of loading direction and sliding failure is smaller, typically about 30 points as indicated in Fig.12 for a typical test, so shorter regressions had to be used and the values of stiffness are more scattered. There was found to be no consistent difference between the stiffnesses at either end of the cycle. Despite the data scatter, interesting trends can be seen, and in Fig.13a there is a clear increase of stiffness with normal load level, which is consistent with the gradient expected from Mindlin & Deresiewicz, although the absolute values are very different, much as Nardelli & Coop (2019) found for quartz sands. The monotonic stiffnesses tend to be slightly lower than the cyclic as they should be, given that the cyclic stiffnesses are for unloading while the monotonic ones are for first loading. However, Fig.13b indicates that there is only a small further increase in stiffness with cycling. Wong & Coop (2020) had found a significant influence of the immersion of the particles in water on the sliding µ values. Data points are shown for the immersed samples in Fig.13b and it is clear that the stiffnesses are not affected significantly.

Cyclic Normal Loading and Pre-Sliding Lateral Loading

Test SC14 investigated cyclic normal loading. The cycles started after monotonic normal loading to 30N and should ideally have cycled from 30N to 10N, although some poor control of the test meant that these values drifted slightly; control of a cyclic force on such a rigid interface is technically difficult using linear actuators. The stiffnesses (Fig.14b) are quantified as secants taken between the bottom and top of each cycle on Fig.14a. There is a significant increase of stiffness on the first cycle compared to the secant stiffness between 10-30N on the first loading, emphasising that the behaviour during first loading is not elastic. But for subsequent cycles, the stiffness is relatively stable, slightly decreasing in the first twenty or so cycles. The vertical displacement continues to increase, and the size of the loops reduces so that the energy loss factor (defined in Fig.14c) also reduces, although it seems it may be starting to stabilise at about 100 cycles (Fig.14d).

In pre-sliding lateral cyclic loading (Fig.15) the size of the loops was fixed at ±50µm and so with symmetrical loading, the overall lateral displacement does not migrate. In this case, the

secant stiffness again increases compared to the pre-cycling monotonic stiffness for loading from 0-50μm, but then, in contrast to normal loading, the stiffness continues to increase stabilising at around 20 cycles. As for normal loading, the loop size reduces, so that the energy loss factor reduces, and for lateral loading, it stabilises again at about 20 cycles.

Conclusion

The research described in this paper aims to provide the input for a future comprehensive "Avatar" model of a commonly used UK railway ballast. Even if the tests were not specifically designed to replicate in-situ conditions, not least only using small numbers of cycles because of apparatus limitations, the work highlights a number of points that may be of practical interest. It is the common practice to improve ballast performance by periodic tamping, and while the benefits of densifying the ballast are clear, the work presented here does highlight how the loss of existing particle contacts would have some detrimental effects. Firstly, as Wong & Coop (2020) highlighted, inter-particle μ values tend to increase with repeated sliding shearing, but also shown here is the developing interlocking between particles which would also be lost.

In normal loading new contacts are very much softer than the simple Hertz model predicts, because of the roughness of the particles. Elastic models that include the effects of roughness such as Greenwood et al. (1984) do give more accurate stiffnesses at smaller normal loads but they cannot capture the plasticity of the displacements which appears at larger loads and is evident in the greater stiffness both in unloading and at the start of the cyclic normal loading. They are also unable to capture creep or contact ageing effects. In lateral loading, the stiffness increased both when comparing the first monotonic loading to the stiffnesses in cyclic pre-failure loading and also between monotonic loading and the stiffnesses at reversals of large displacement cycles. In the large displacement cycles, the stiffnesses showed little further change after the first cycle, while in pre-failure cycling in lateral and normal loading the cyclic stiffnesses stabilised after a few tens of cycles. Creep (contact ageing) was found to take a few days to a few weeks to stabilise. All of the effects of cycling and/or creep would also be re-established for new contacts.

Other key conclusions arising from this research have been that the Mindlin & Deresiewicz model for lateral loading overpredicts the stiffnesses by more than an order of magnitude, possibly because of the effect of roughness, but even current suggestions of the possible

influence of roughness grossly underestimate its effect. However, the load level effect on stiffness that arises from this type of model is consistent with the data. The presence of water does not have a significant effect on stiffness. While short-lived contact ageing can be seen at pre-failure states, there was no rate effect on sliding failure.

Out of the very large range of contact models available, the work has focussed on the success of ones currently commonly used in geotechnical DEM analyses. While experimental work on smaller and smoother natural sand particles (Nardelli & Coop, 2019) has highlighted that these current models might be applied to many DEM analyses of sands with little or no modification, they are very far from being suitable for the crushed rock tested here and we will need either to make large modifications to them or more likely adopt completely different models probably focussing not only on the roughness but also on plasticity at the asperity scale.

For the granitic ballast tested the contact radii of the points of the angular ballast particles do not show a large variation and are probably controlled by the crystal size of the rock. Within any assembly of particles, there will be a much greater variety of radii at the contacts made between particles, and the contact stiffnesses will vary accordingly. It is also likely that other ballasts and rock fills will have substantially different contact radii according to how they break as they are crushed, their crystal or particle size and whether they are crystalline or clastic.

Acknowledgements

References

Afrouz, A. A. (1992) Rock mass classification systems and modes of ground failure. CRC Press.

Brace, W. F. (1965). Some new measurements of linear compressibility of rocks. J. Geophysical Research, 70(2), 391-398.

Cavarretta, I., Coop, M. R. & O'Sullivan, C. (2010). The influence of particle characteristics on the behaviour of coarse grained soils. Géotechnique 60(6), 413–423, https://doi.org/10.1680/geot.2010.60.6.413.

Chen, Y., Hu, S., Wei, K., Hu, R., Zhou, C., & Jing, L. (2014). Experimental characterization and micromechanical modeling of damage-induced permeability variation in Beishan granite. International Journal of Rock Mechanics and Mining Sciences, 71, 64-76.

Cole, D. M. (2015). Laboratory observations of frictional sliding of individual contacts in geologic materials. Granular Matter, 17(1), 95-110. http://doi:10.1007/s10035-014-0526-0.

Cole, D. M., Mathisen, L. U., Hopkins, M. A., & Knapp, B. R. (2010). Normal and sliding contact experiments on gneiss. Granular Matter, 12(1), 69-86. https://doi:10.1007/s10035-010-0165-z.

Cole, D. M., & Peters, J. F. (2007). A physically based approach to granular media mechanics: grain-scale experiments, initial results and implications to numerical modeling. Granular Matter, 9(5), 309-321. https://doi:10.1007/s10035-007-0046-2.

Domede, N., Parent, T., & Sellier, A. (2019). Mechanical behaviour of granite: a compilation, analysis and correlation of data from around the world. European J. Env. & Civil Eng., 23(2), 193-211.

Fellerec, J. & McDowell, G. (2010). Modelling realistic shape and particle inertia in DEM. Géotechnique 60(3), 227–232, https://doi.org/10.1680/geot.9.T.015.

Greenwood, J. A., Johnson, K. L. & Matsubara, E. (1984). A surface roughness parameter in Hertz contact. Wear 100, No. 1–3, 47–57.

Hertz, H. (1882). Ueber die Berührung fester elastischer Körper. Journal für die reine und angewandte Mathematik, 92, 156-171.

Jaeger, J. C., Cook, N. G., & Zimmerman, R. (2009). Fundamentals of rock mechanics. John Wiley & Sons.

Johnson, K.L. (1985). Contact Mechanics. Cambridge, Cambridge University Press.

Kasyap, S.S. & Senetakis, K. (2019) Experimental Investigation of the Coupled Influence of Rate of Loading and Contact Time on the Frictional Behavior of Quartz Grain Interfaces under Varying Normal Load. Int. J. Geomechanics, 19(10).

Le Pen, L., Ahmed, S., Zervos, A., Harkness, J. & Powrie, W. (2014) Resin recovery and the use of computed tomography for quantitative image analysis of railway ballast. Proc. 2nd Int. Conf. Railway Tech., J. Pombo, (Ed.), Civil-Comp Press, Stirlingshire, Paper 0123456789.

Mavko, G., Mukerji, T., & Dvorkin, J. (2009). The rock physics handbook: Tools for seismic analysis of porous media. Cambridge university press.

Michalowski, R.L., Wang, Z. & Nadukuru, S.S. (2018) Maturing of contacts and ageing of silica sand. Géotechnique, 68(2), 133–145.

Mindlin, R. D. & Deresiewicz, H. (1953). Elastic spheres in contact under varying oblique forces. Trans. ASME, J. Appl. Mech. 20, 327–343.

Nardelli, V. & Coop, M.R. (2019) The experimental contact behaviour of natural sands: normal and tangential loading. Géotechnique. 69(8), 672-686.

Nardelli, V., Coop, M. R., Andrade, J. E. & Paccagnella, F. (2017) An experimental investigation of the micromechanics of Eglin sand. Powder Technol. 312, 166–174.

Otsubo, M., O'Sullivan, C., Sim, W.W. & Ibraim, E. (2015). Quantitative assessment of the influence of surface roughness on soil stiffness. Géotechnique 65(8), 694-700.

Procter, D. C. & Barton, R. R. (1974). Measurements of the angle of interparticle friction. Géotechnique 24(4), 581–604, https://doi.org/10.1680/geot.1974.24.4.581.

Senetakis, K., Coop, M. R., & Todisco, M. C. (2013). Tangential load–deflection behaviour at the contacts of soil particles. Géotechnique Letters, 3(2), 59-66. https://doi:10.1680/geolett.13.00019.

Skinner, A. E. (1969). A note on the influence of interparticle friction on shearing strength of a random assembly of spherical particles. Géotechnique 19(1), 150–157, https://doi.org/10.1680/geot.1969.19.1.150.

Tabor, D. (1951) The Hardness of Metals. Oxford University Press.

Tapias, M., Alonso, E.E. & Gili, J. (2015) A particle model for rockfill behaviour. Géotechnique, 65(12), 975-994.

Vasconcelos, G., Lourenço, P. B., Alves, C. A. S., & Pamplona, J. (2008). Ultrasonic evaluation of the physical and mechanical properties of granites. Ultrasonics, 48(5), 453-466.

Vu-Quoc, L. & Zhang, X. (1999) An accurate and efficient tangential force-displacement model for elastic frictional contact in particle-flow simulations. Mechanics of Materials 31, 235-269.

Wong, C.P.Y., Boorman, B. & Coop, M.R. (2018). The construction and commissioning of a new inter-particle loading apparatus for the micromechanical behaviour of railway ballast. Proc. IS Atlanta 2018, Symp. on Geomech. from Micro to Macro in Research and Practice, Atlanta.

Wong, C. P. Y. & Coop, M. R. (2020) Development of inter-particle friction in a railway ballast. Géotechnique Letters, 10(4), 535-541.

Yimsiri, S., & Soga, K. (2000). Micromechanics-based stress-strain behaviour of soils at small strains. Géotechnique, 50(5), 559-571.

Nomenclature

a_H radius of contact area in Hertz (1882)

a^* radius of apparent contact area in Greenwood et al. (1984)

E Young's modulus

E^* equivalent elastic modulus

N normal contact force

R radius of contacting sphere

S_q root mean square roughness

T shear force

T^* shear force at last reversal of loading direction

α normalised asperity size (see Eqn.2)

δ mutual displacement of spheres

η energy loss factor

μ coefficient of friction

ν Poisson's ratio

σ combined roughness

Table 1 Test details (SC single contact, MC multiple contacts)

Test	Normal load (N)	Contacts	Upper particle contact radii in line of displacement / perpendicular (mm)	Dry / immersed	Details
MC	100	Multiple contacts	NA	Dry	Measurement of μ only
SC01	100	Fresh to fresh	1.5/2.0	Dry	
SC02_a	100	Old to fresh	3.1/2.6	Dry	
SC02_b	100	Old to old	3.1/2.6	Dry	
SC03	20	Old to old	2.4/2.2	Dry	
SC04	20	Fresh to fresh	2.1/1.9	Dry	
SC05	20	Fresh to fresh	1.7/2.3	Dry	
SC06	20	Fresh to fresh	1.4/1.5	Dry	
SC07	200	Fresh to fresh	1.3/1.0	Dry	
SC08	100	Fresh to fresh	1.7/1.0	Dry	
SC09	200	Fresh to fresh	2.9/3.2	Immersed after 43 shear cycles	
SC10	200	Old to fresh	2.1/2.1	Immersed after 37 shear cycles	
SC11	100	Fresh to fresh	NA/1.6	Dried after 43 shear cycles	
SC12	20	Fresh to fresh	1.5/NA	Immersed	
SC13_a	100	Fresh to fresh	1.5/1.3	Dry	Pre-sliding failure shear cycles of ±50μm
SC13_b	100	Old to fresh	1.5/1.3	Dry	2mm shear cycles after SC13_a on the same particles
SC14_a	200	Fresh to fresh	3.4/4.4	Dry	Normal load cycles 10N-30N. Creep at N=55N and 200N. Creep at N=200N & T=100N

SC14_b	200	Old to fresh	3.4/4.4	Dry	2 and 1.2mm shear cycles after SC14_a on the same particles. Shear cycles with periods of 0.5, 50 and 0.5 hrs.
SC15	100	Fresh to fresh	4.4/5.5	Dry	Normal load-unload cycles up to 20, 50 and 100N.

(a)

R=1.3mm

5mm
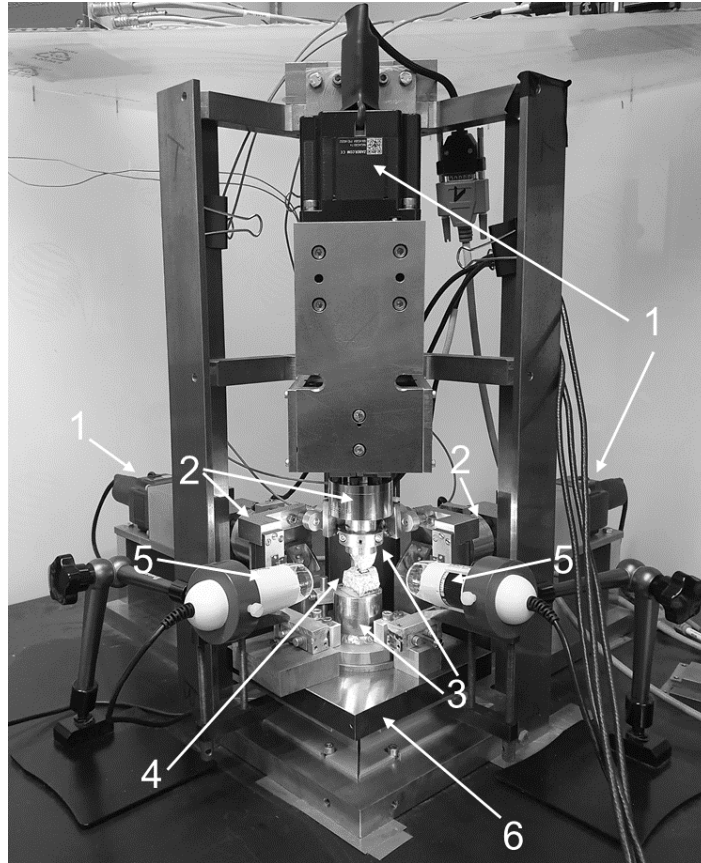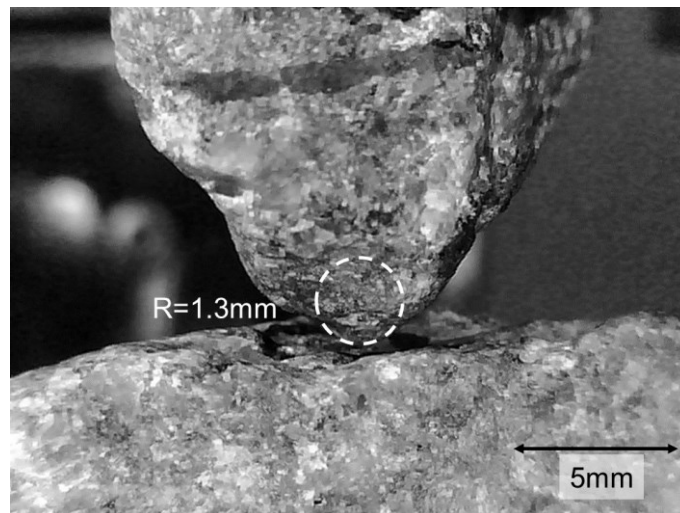
(b)

Fig.1 Experimental apparatus (a) general view of the inter-particle loading apparatus (1 linear actuators, 2 load cells, 3 platens, 4 particles, 5 digital microscope cameras, 6 sled on three-point bearing system), (b) a microscope camera image of a pair of particles mounted on the platens.
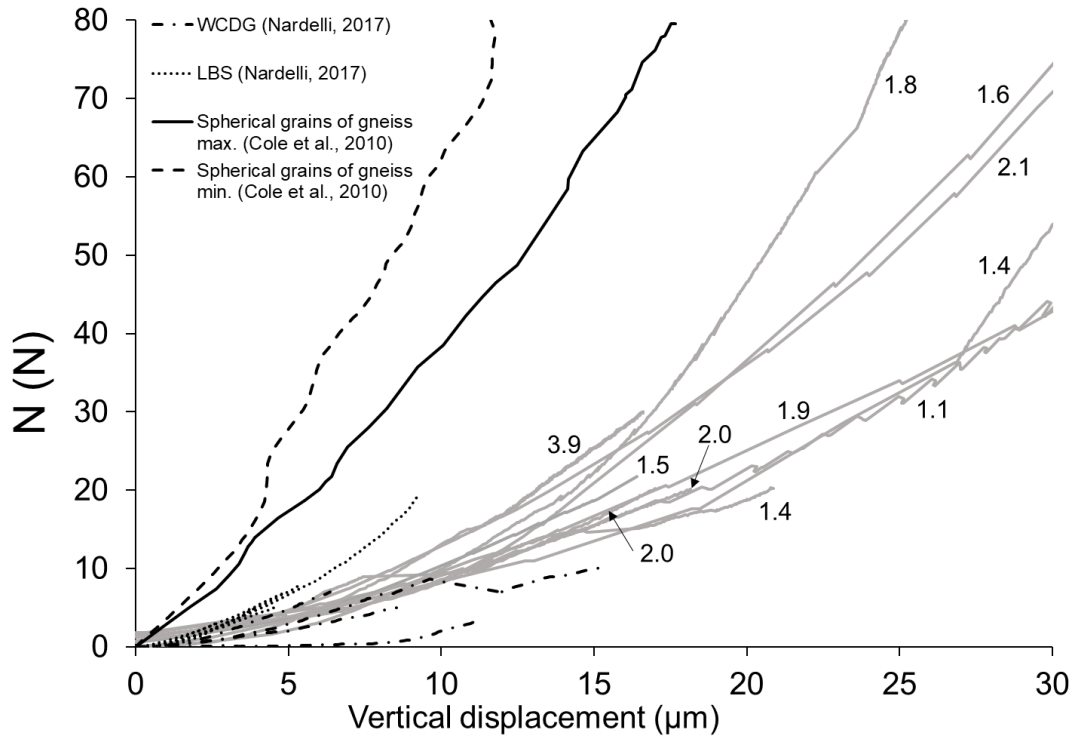
Fig.2 Normal load-deformation curves for the ballast compared a decomposed granite (WCDG) and Leighton Buzzard sand (LBS) from Nardelli & Coop (2019), and spherical grains of gneiss from Cole et al. (2010) **(labels indicate the radius of upper particle contact).**
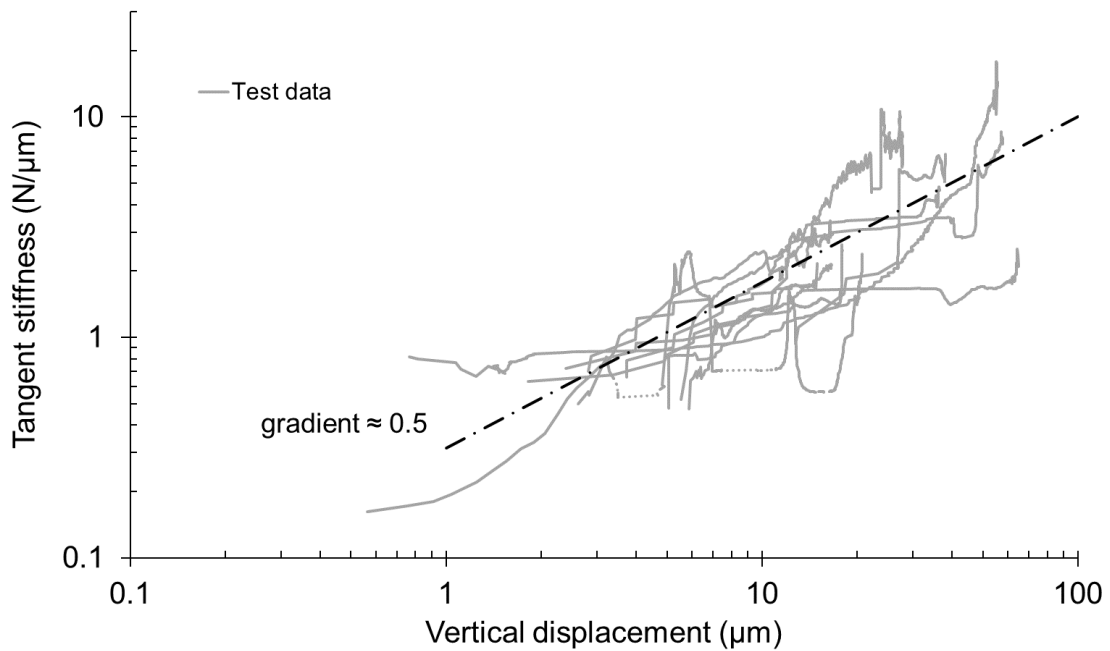
Fig.3 Tangent stiffness-deformation curves for normal loading.
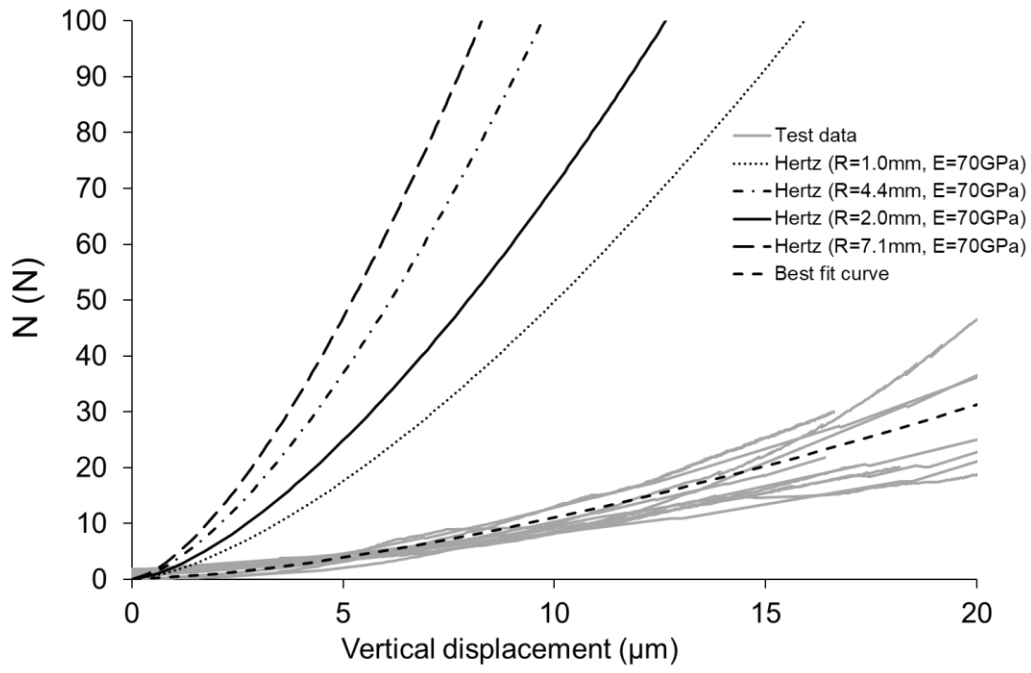
(a)
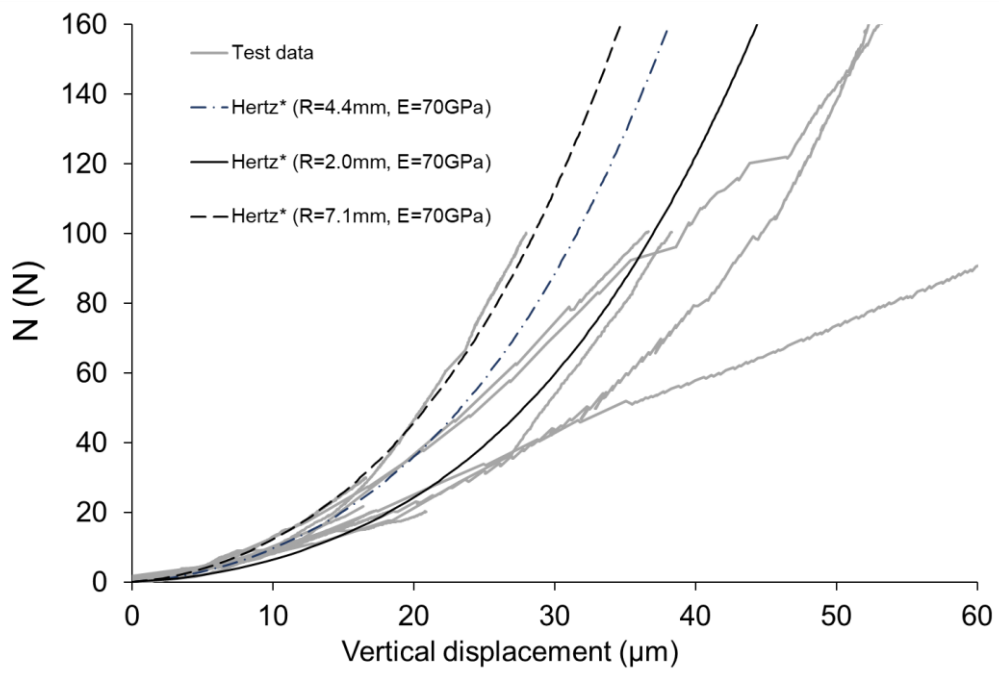
(b)
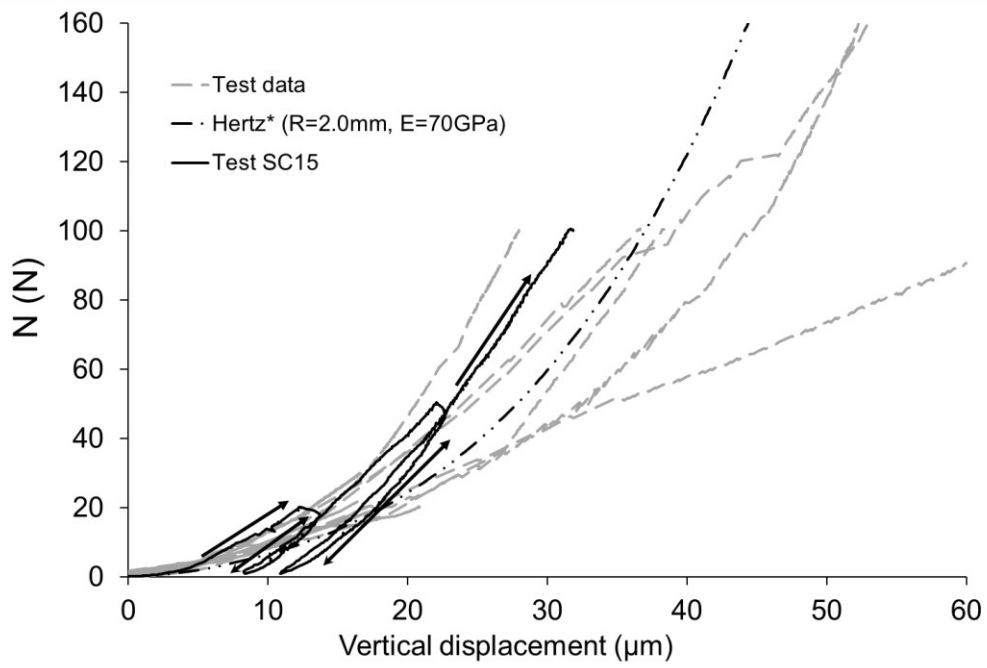
(c)

Fig.4 Comparison between test data and (a) Hertz (1882) for different contact radii, (b) Hertz modified for roughess (Hertz*, Greenwood et al., 1984), (c) unload-reload loops for Test SC15.
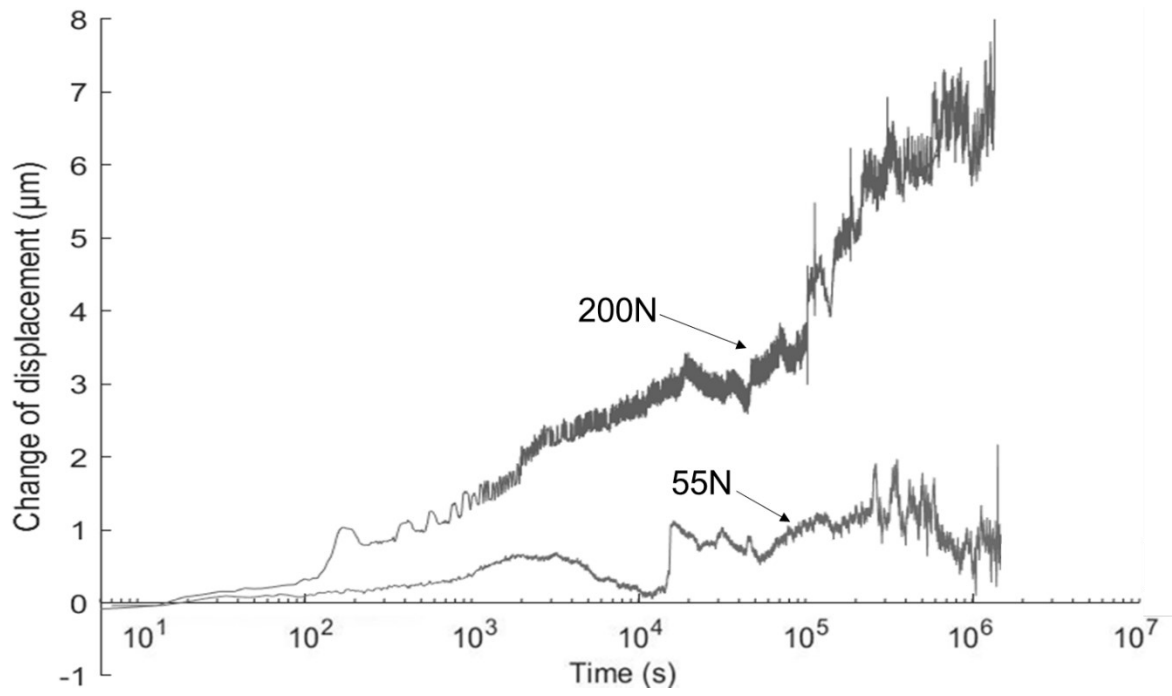
(a)
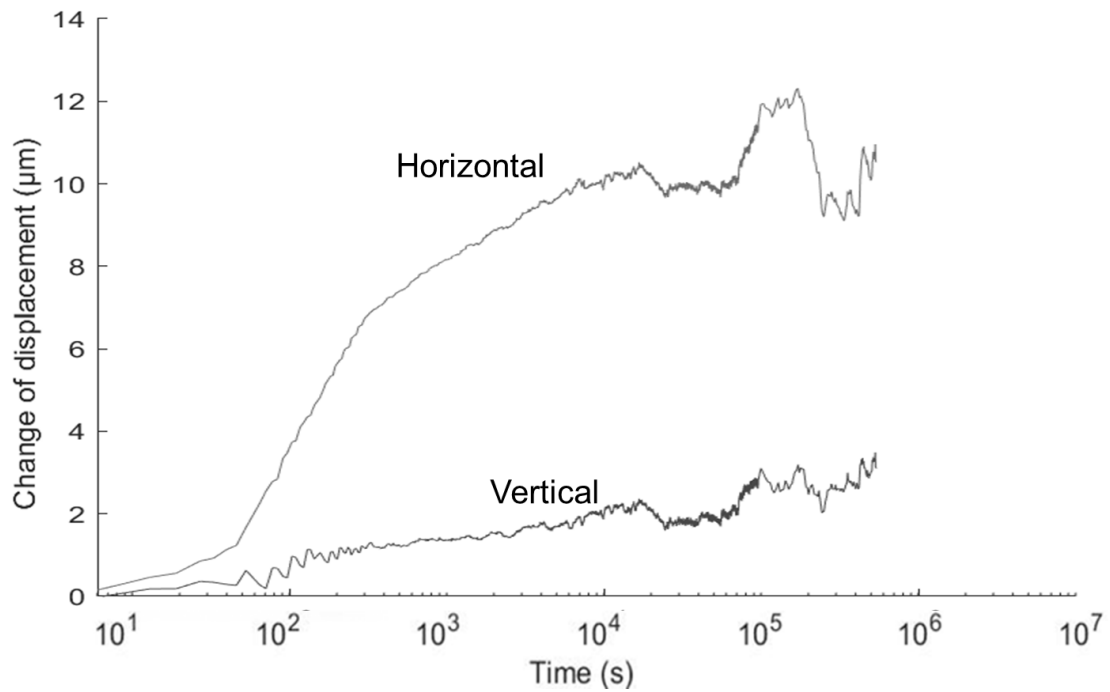
(b)

Fig.5 Contact ageing under (a) normal loads only, and (b) a combined normal load of 200N and shear load of 100N (Test SC14_a).
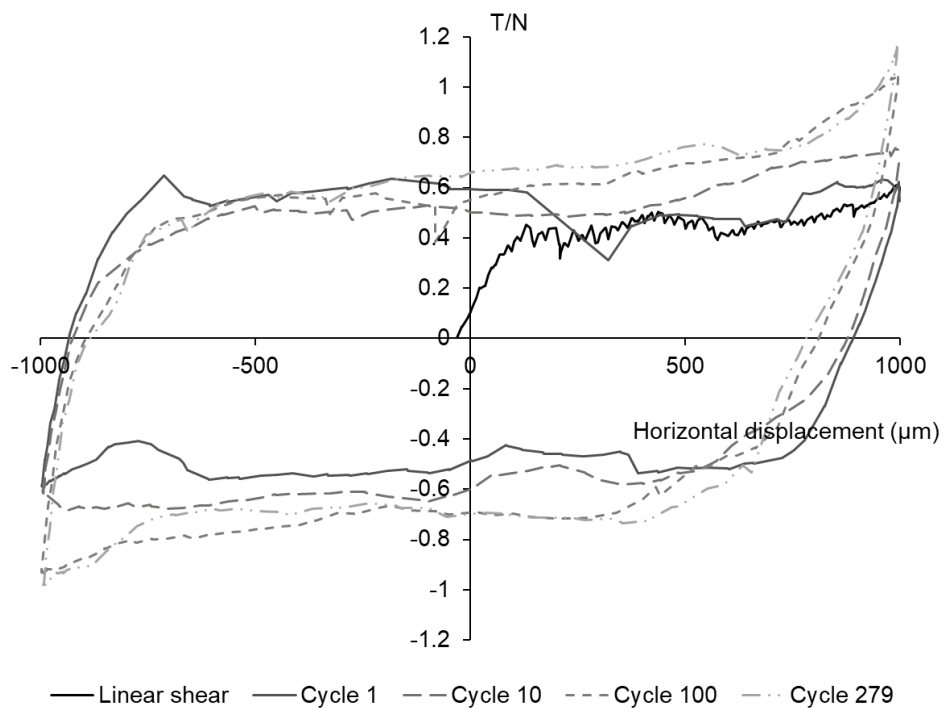
(a)
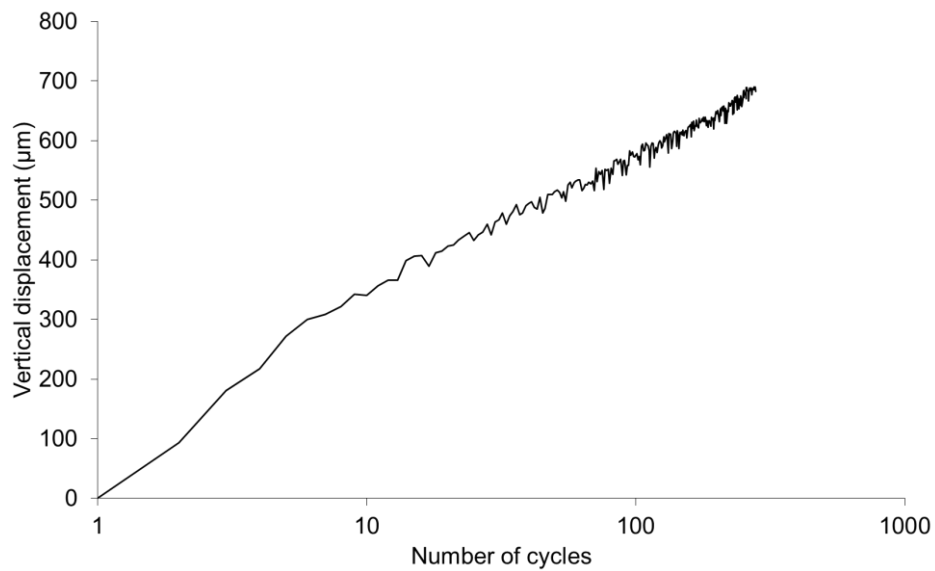
(b)

Fig.6 Cyclic shearing results of Test SC13_b, (a) ratio of shear to normal force for linear shear stage and cycles 1, 10, 100 and 279, (b) vertical displacement at the centre of the cycle.
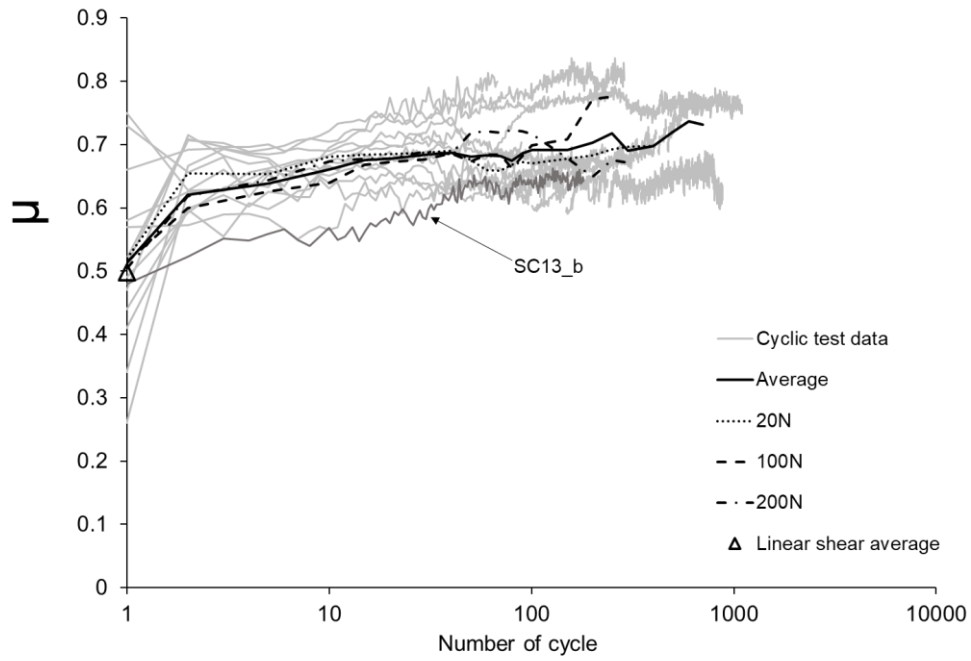
(a)
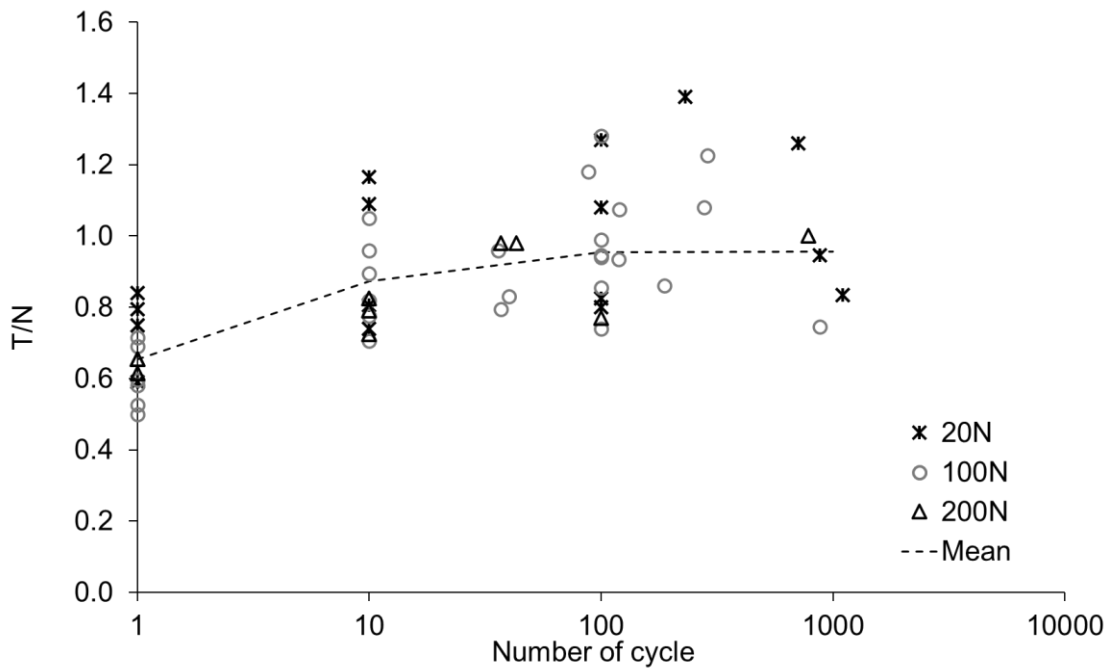
(b)

Fig.7 Evolution of contact resistance to shear under large displacement cycling (a) average inter-particle friction coefficients (μ) for dry contacts (modified from Wong & Coop, 2020), (b) T/N values at the corners of the displacement cycles.
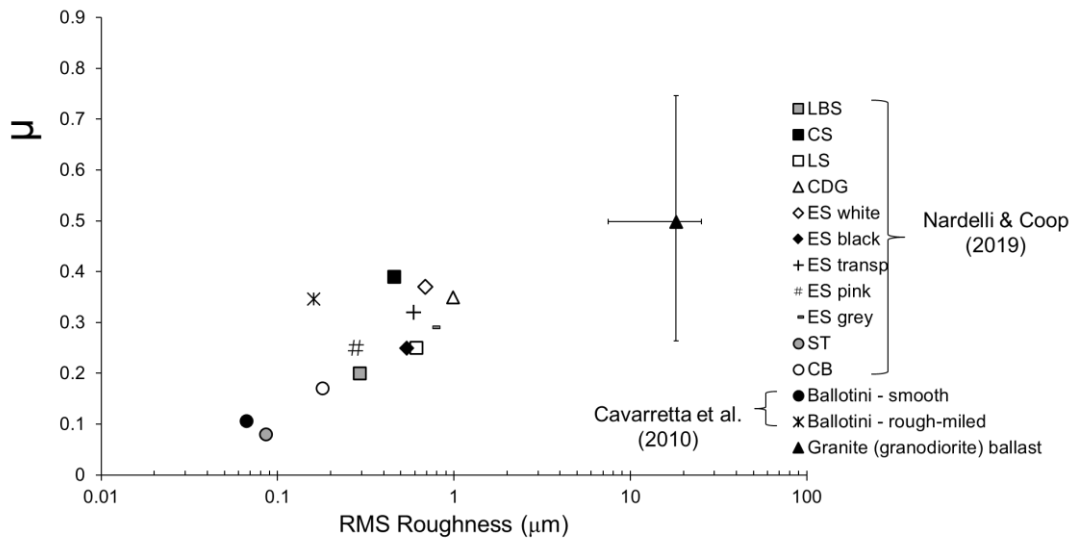
Fig.8 Effect of roughness (S_q RMS) on inter-particle friction coefficients for the monotonic shearing of different materials (NB measured range of values shown for granite ballast; CS: carbonate sand, LS: crushed limestone, CDG: completely decomposed granite, ES: Eglin sand, ST: chrome steel balls, CB: ceramic balls; modified from Nardelli & Coop, 2019, with ballast data and data for ballotini from Cavarretta et al., 2010).
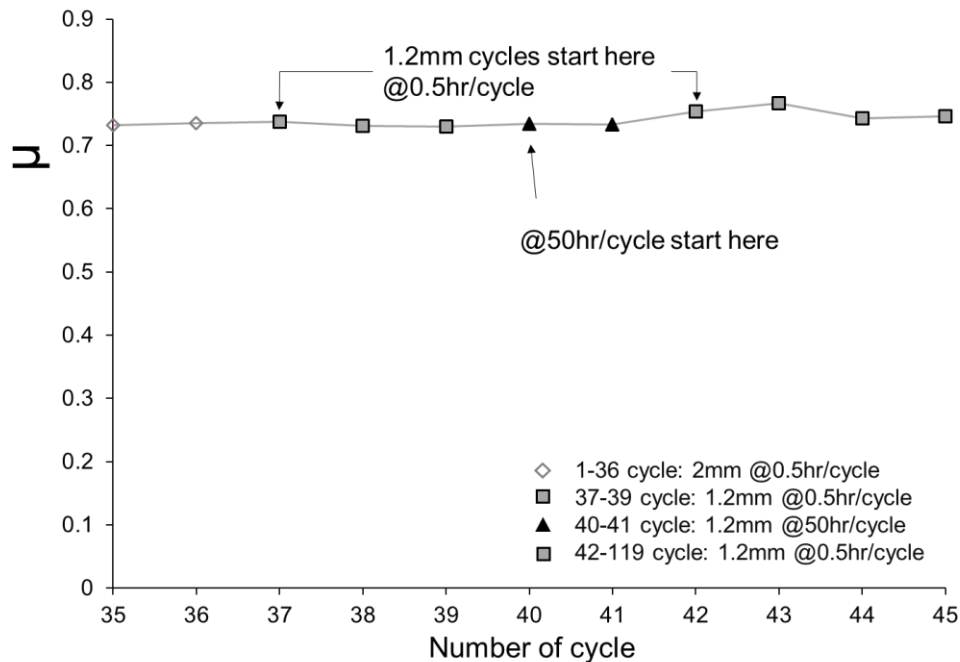
Fig.9 The influence of the rate of cyclic sliding on the inter-particle friction coefficient (Test SC14-b).
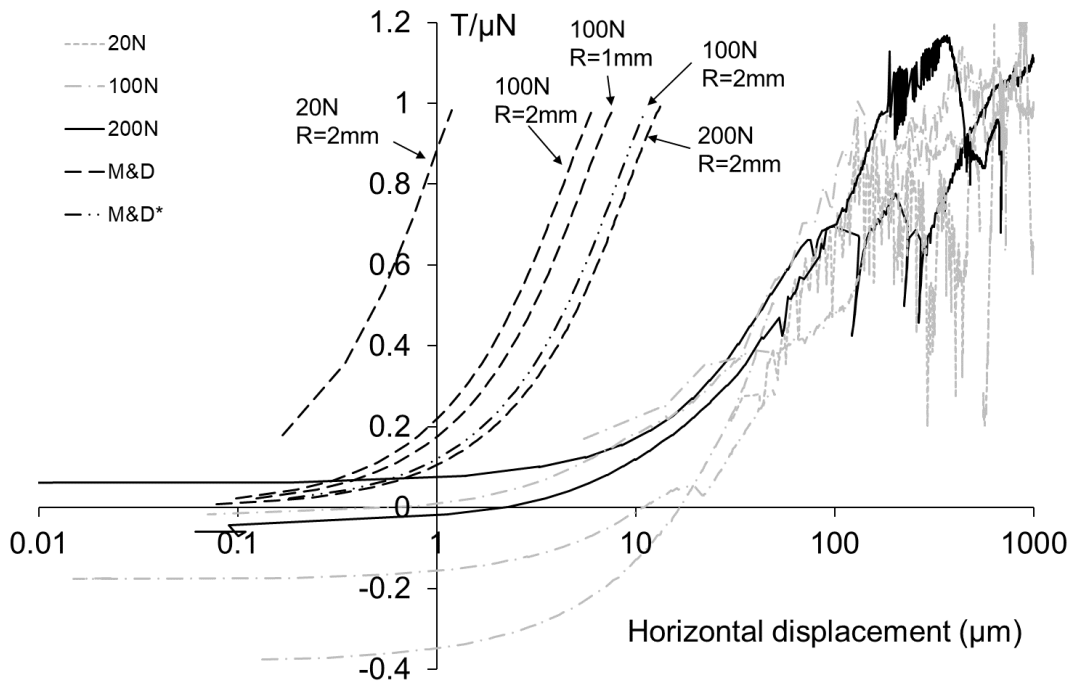
Fig.10 Comparison between test data and the theoretical curves obtained from the Mindlin and Deresiewicz (1953) (M&D) model for lateral loading (M&D* modified M&D for roughness).
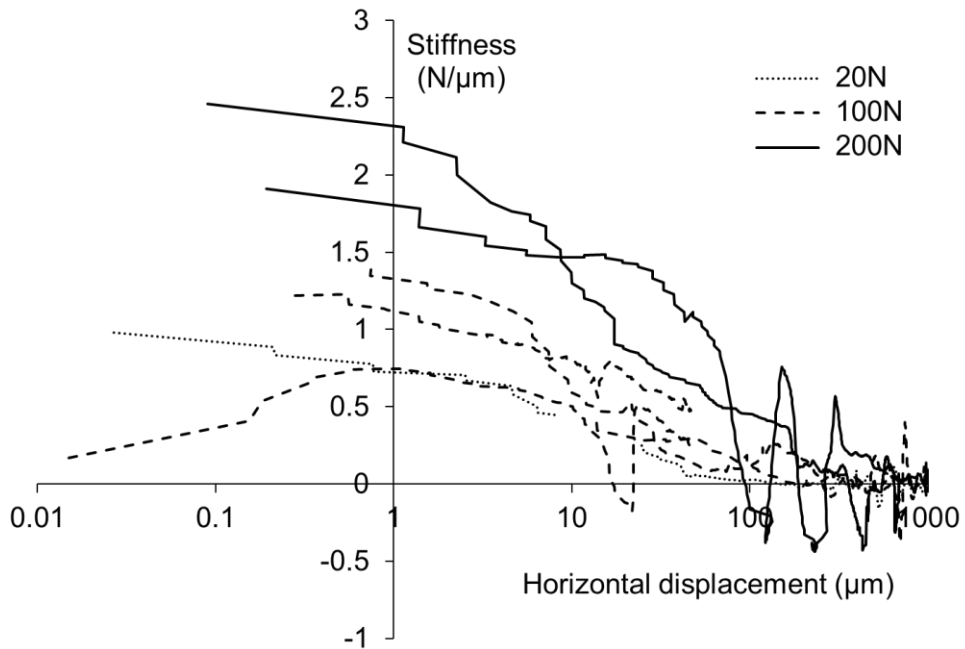
Fig. 11 Tangent stiffnesses for monotonic shear loading.
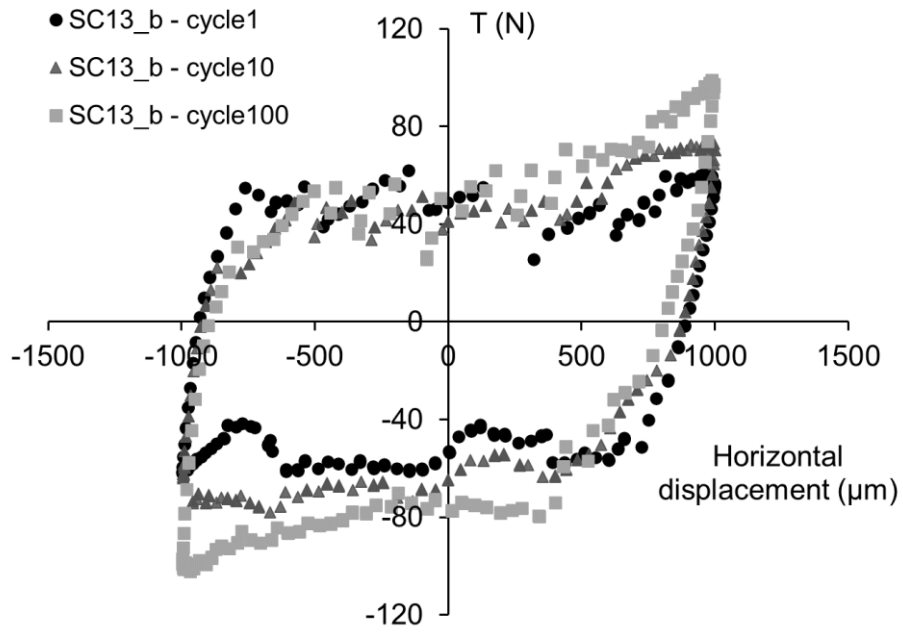
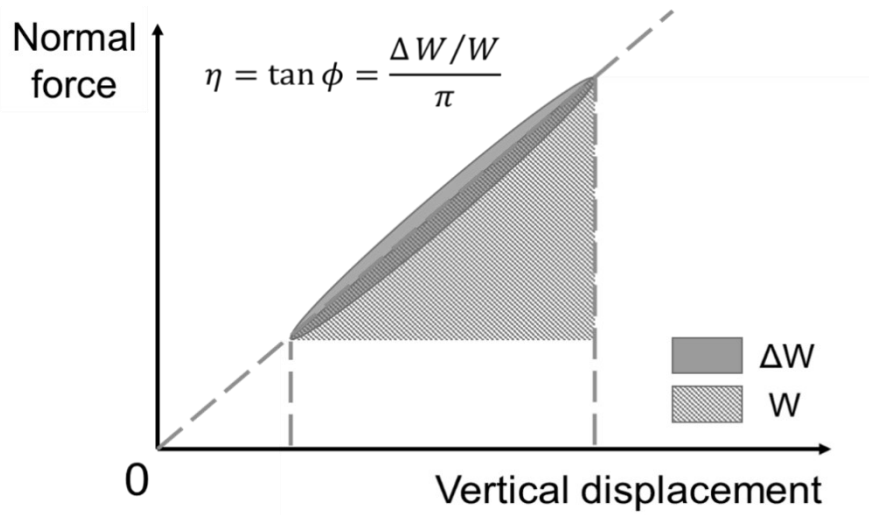Fig.12 Cyclic shearing results of Test SC13_b for cycles 1, 10 and 100.
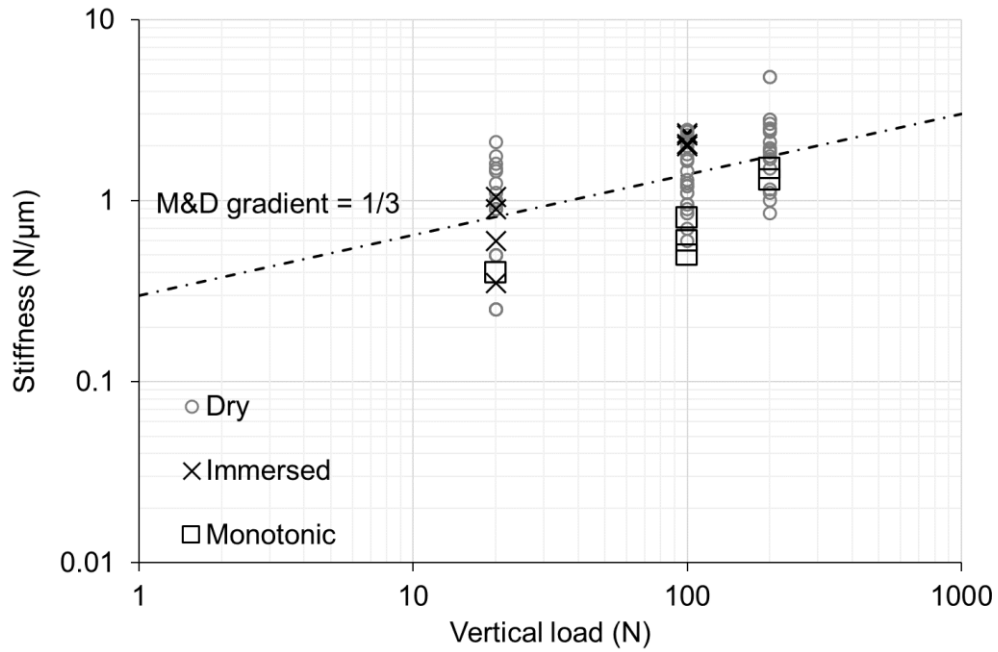
(a)
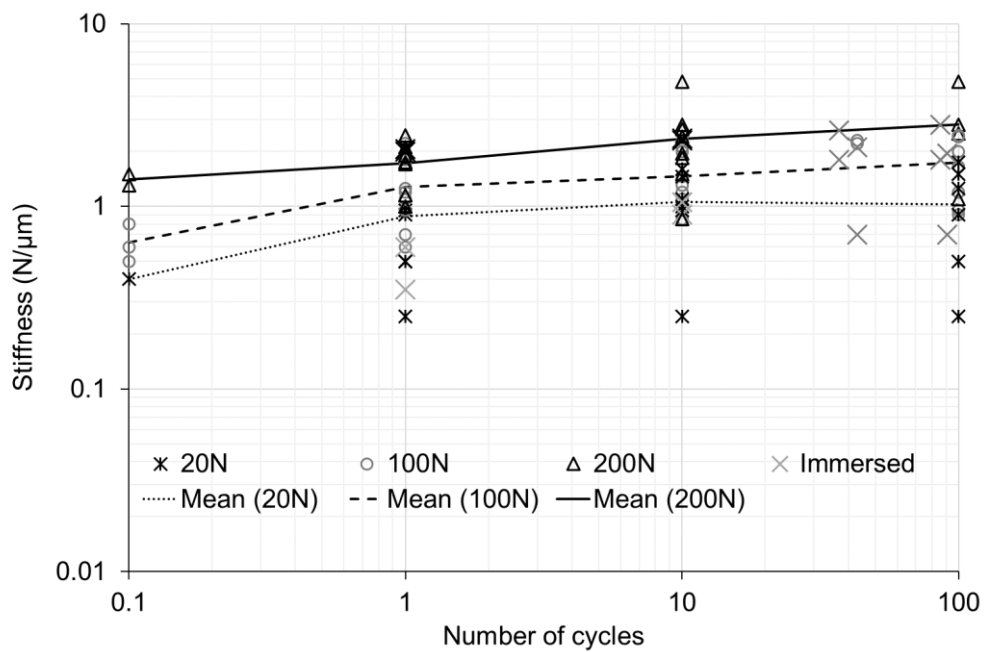
(b)

Fig.13 Lateral stiffnesses at a displacement of 10µm (a) effect of vertical load, (b) effect of load cycle (monotonic data are plotted at 0.1 cycles).
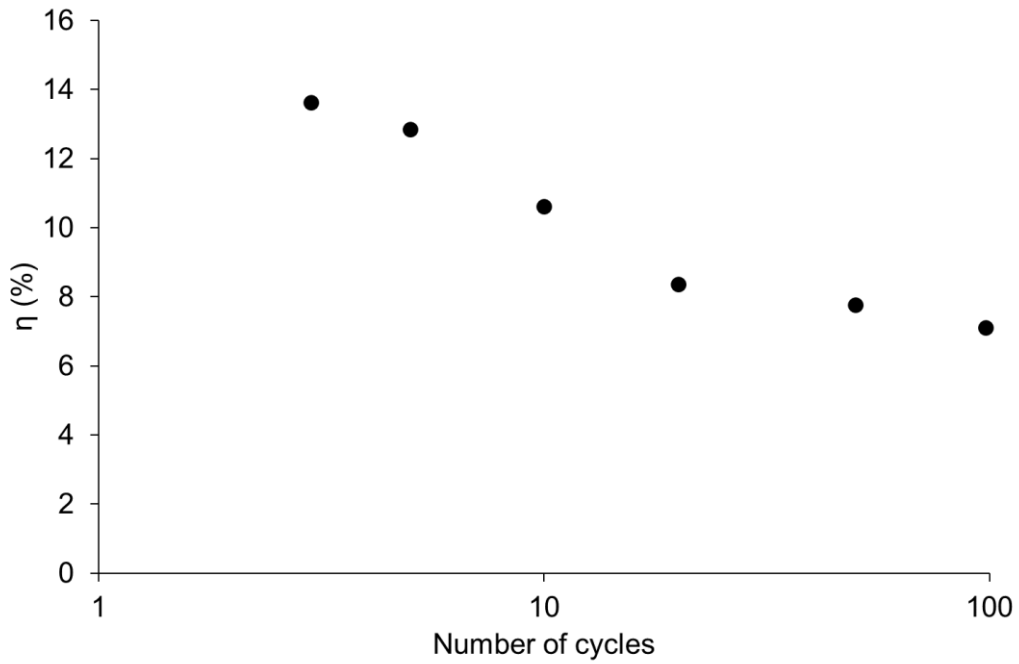
(a)
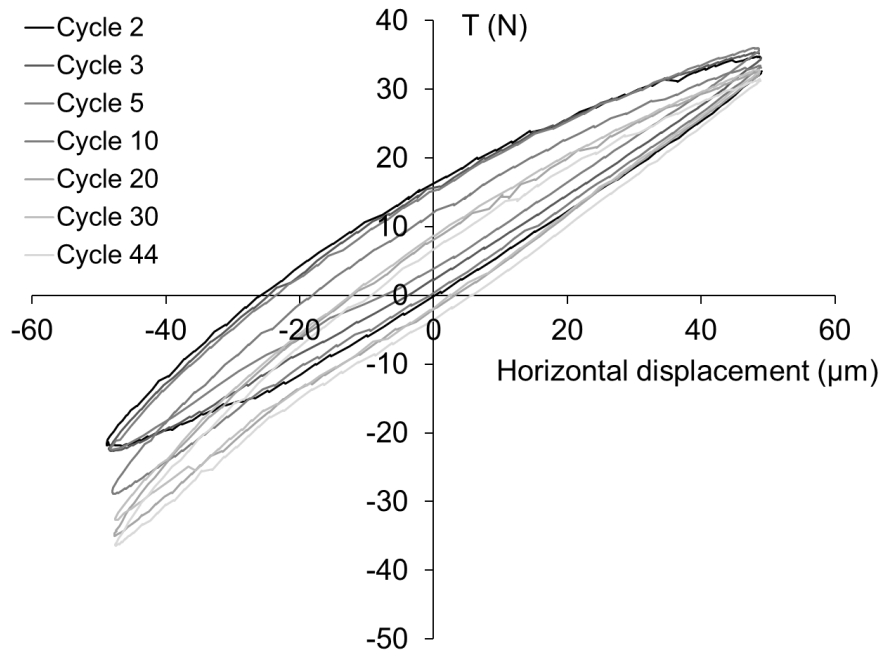

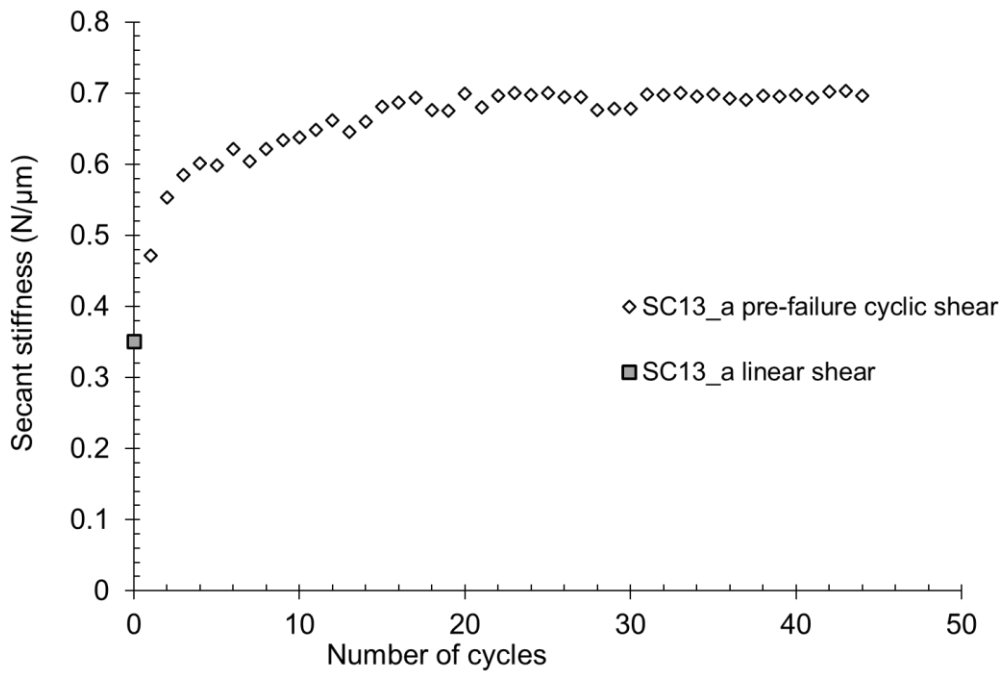
(b)
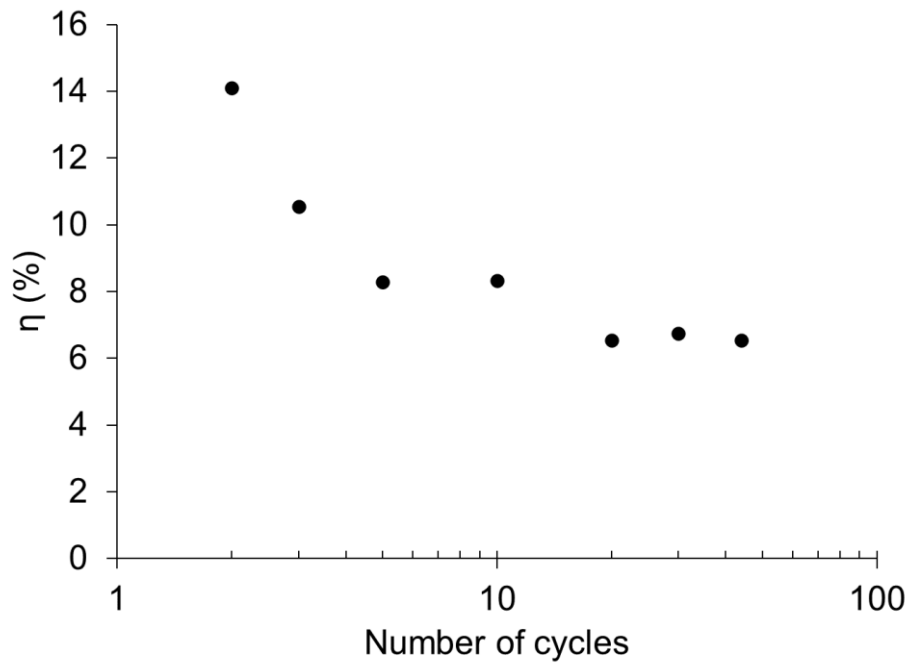
$$\eta = \tan\phi = \frac{\Delta W/W}{\pi}$$
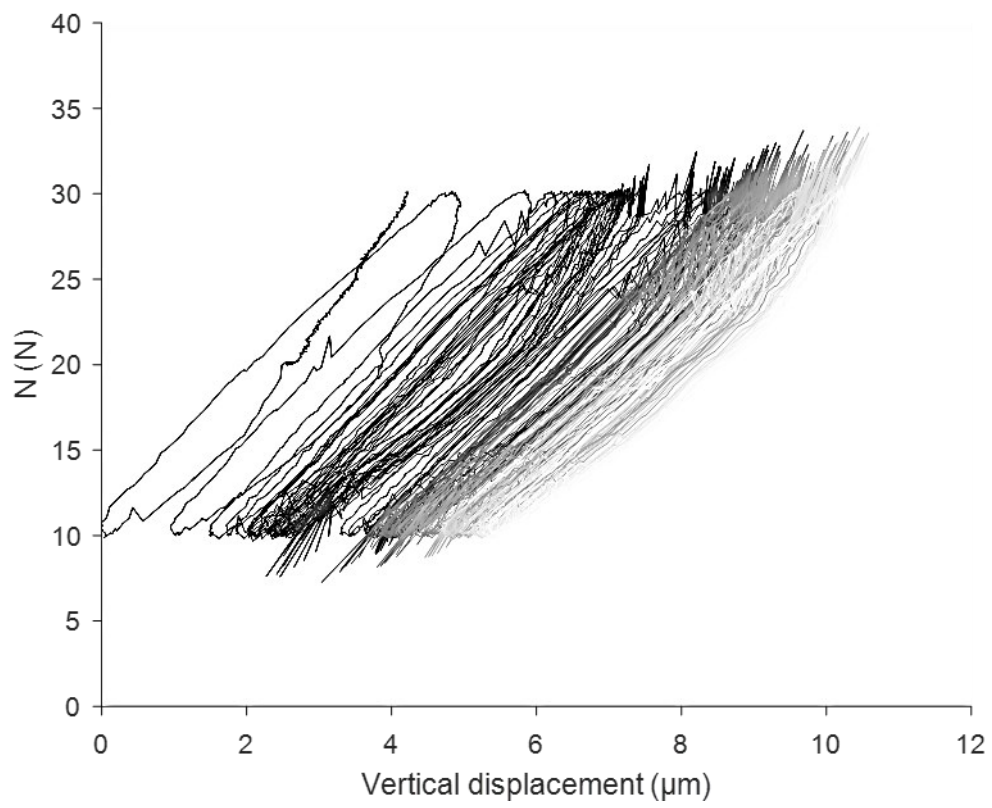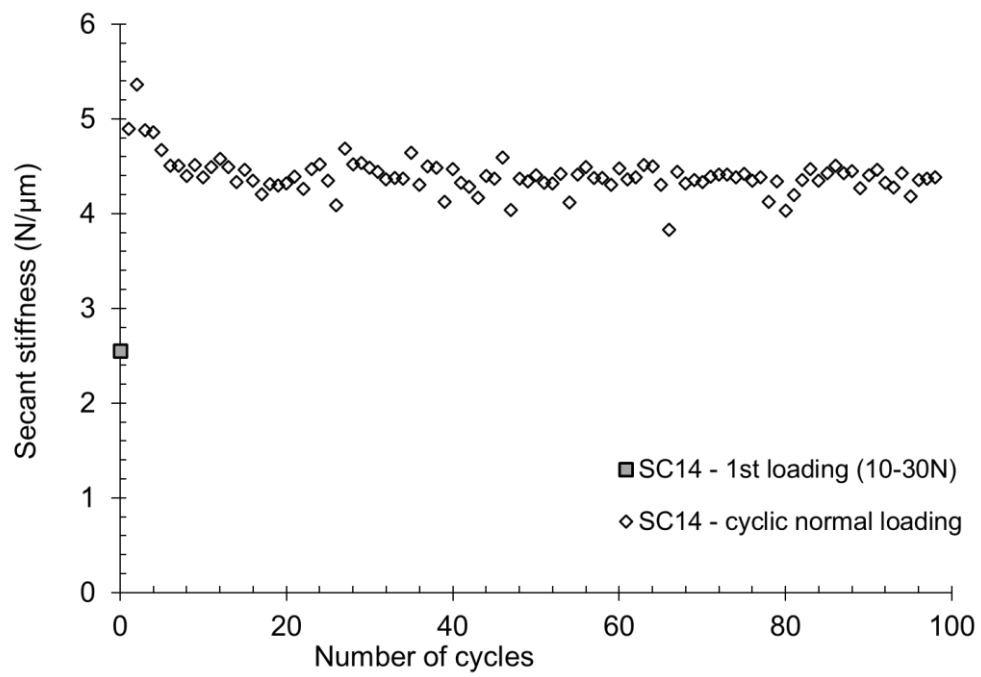
(c)

(d)

Fig.14 Cyclic normal loading of Test SC14: (a) normal load-displacement curves, (b) secant stiffnesses, (c) definition of energy loss factor η, (d) energy loss factor for selected loops.

(a)

(b)

(c)

Fig.15 Pre-failure cyclic shearing for Test SC13_a: (a) tangential load-displacement curves of selected cycles (b) secant stiffnesses for all cycles, (c) energy loss factor η for the selected loops.